AGU PUBLICATIONS

JGR

Journal of Geophysical Research: Oceans

RESEARCH ARTICLE

10.1002/2016JC011694

Special Section:
Dense water formations in the North Western Mediterranean: from the physical forcings to the biogeochemical consequences

Estimating dense water volume and its evolution for the year 2012–2013 in the Northwestern Mediterranean Sea: An observing system simulation experiment approach

Robin Waldman[1], Samuel Somot[1], Marine Herrmann[2], Pierre Testor[3], Claude Estournel[4], Florence Sevault[1], Louis Prieur[5], Laurent Mortier[6], Laurent Coppola[5], Vincent Taillandier[5], Pascal Conan[7], and Denis Dausse[3]

[1]Centre National de Recherches Meteorologiques, Meteo-France-CNRS, Toulouse, France, [2]Laboratoire d'Etudes Geophysiques et d'Oceanographie Spatiale, UMR5566, CNRS-CNES-IRD-Universite de Toulouse, Toulouse, France, [3]Centre National de Recherches Scientifiques, Universite Pierre et Marie Curie, Laboratoire d'Oceanographie et de Climat—Experimentations et Approches Numeriques, Paris, France, [4]Laboratoire d'Aerologie, Observatoire Midi-Pyrenees, Toulouse, France, [5]Laboratoire d'Oceanographie de Villefranche-sur-Mer, Villefranche-sur-Mer, France, [6]ENSTA ParisTech, Universite Paris-Saclay, Palaiseau, France, [7]Observatoire Oceanologique de Banyuls-sur-Mer, Banyuls-sur-Mer, France

Key Points:
- MOOSE observing network is able to estimate convection with high accuracy
- 2012–2013 was an exceptional dense water formation and restratification year
- Dense water volume is maximum in spring 2013 and he west of the basin dominates its evolution

Correspondence to:
R. Waldman,
robin.waldman@meteo.fr

Citation:
Waldman, R., et al. (2016), Estimating dense water volume and its evolution for the year 2012–2013 in the Northwestern Mediterranean Sea: An observing system simulation experiment approach, *J. Geophys. Res. Oceans*, *121*, doi:10.1002/2016JC011694.

Received 2 FEB 2016
Accepted 12 AUG 2016
Accepted article online 19 AUG 2016

Abstract The Northwestern Mediterranean (NWMed) Sea includes one of the best observed ocean deep convection sites in the World. An observing system simulation experiment (OSSE) is developed to provide a methodology for estimating observing network errors. It is applied to quantify dense water volumes in the NWMed during 2012–2013 with their observation error from MOOSE network. Results from the OSSE show low spatiotemporal sampling errors, which confirms MOOSE network ability to measure dense waters. However, results are highly sensitive to instrumental stability. The dense water volume is then estimated in observations from four ship cruises between summers 2012 and 2013. A large seasonal cycle is found, maximal in spring 2013 and dominated by the area west of 6.5°E. The dense water volume ($\sigma_0 > 29.11\,kg/m^3$) is stable between summer 2012 ($13.3\pm0.6 \times 10^{13}\,m^3$) and winter 2013 ($13.7\pm1.3 \times 10^{13}\,m^3$). It increases dramatically in spring 2013 ($17.7\pm0.9 \times 10^{13}\,m^3$) due to an intense convective event, and it finally decreases rapidly in summer 2013 ($15.1\pm0.6 \times 10^{13}\,m^3$) due to restratification and spreading. We estimate an open-sea dense water formation (DWF) rate of 1.4 ± 0.3 Sv between summer 2012 and spring 2013 over the studied area, extrapolated to 2.3 ± 0.5 Sv over the whole NWMed Sea and for the optimal timing. This is to our knowledge the highest measured DWF rate, suggesting winter 2013 was exceptionally convective. The observed restratification rate between spring and summer 2013 is -0.8 ± 0.4 Sv. This study provides robust quantifications of deep convection during an exceptional event that will allow to evaluate numerical simulations.

1. Introduction

1.1. Climatological and Biogeochemical Importance of Deep Convection

The Northwestern Mediterranean (NWMed) Sea is a key region of dense water formation (DWF) in the World ocean [*Marshall and Schott*, 1999]. The rate of formation of deep waters and in particular western Mediterranean deep water (WMDW), the main deep water mass in the NWMed, constrains many biogeochemical and thermodynamical processes: nutrient renewal in upper layers and biological activity [*Herrmann et al*., 2013; *Auger et al*., 2014; *Tamburini et al*., 2013], carbon and heat storage rate [*Santinelli et al*., 2013; *Winton et al*., 2013; *Rugenstein et al*., 2013], and therefore climate.

Ocean deep convection also plays a key role in activating the thermohaline circulation, both at regional and global scales. In the Mediterranean Sea [*Crépon et al*., 1989] showed analytically that a thermodynamical forcing comparable to that of the convective region induces an intensifying geostrophic flow around the convective region. *Herrmann et al*. [2009] showed from a modeling study that the winter sea surface height (SSH) minimum at the convective region, associated with a cyclonic gyre current, is highly correlated to deep convection intensity. As for deep currents, *Schroeder et al*. [2008a] show the spreading of an [O_2] anomaly in the Algerian basin on the year following the exceptional 2004–2005 convective winter,

suggesting a rapid basin-scale spreading of newly formed deep waters. *Canals et al*. [2007] show the link between dense water cascading in the NWMed and high-suspended sediment concentration near the seabed. Finally, *Naranjo et al*. [2014] suggest from a modeling study that the interannual variability of Mediterranean outflow water at the strait of Gibraltar is related to the magnitude of deep convection at the Gulf of Lions.

Therefore, estimating quantitatively ocean deep convection and deep water mass transformations is a major challenge for observation networks devoted to the study of physical processes and biogeochemical cycles and also for ocean modeling.

1.2. Deep Convection Estimates in the NWMed Sea

Ocean deep convection occurs in the NWMed Sea when the ocean stratification becomes null under the effect of intense surface buoyancy (mostly heat) fluxes [*Mertens and Schott*, 1998]. It involves the vertical mixing of the ocean column by small plumes that contribute to ventilate the deep ocean, rapidly altering its physical and biogeochemical properties which otherwise evolve very slowly [*Marshall and Schott*, 1999]. This process can be quantified by estimating the total volume implied in deep convection or equivalently, a yearly deep convection rate can be deduced by dividing the convected volume by the number of seconds in 1 year [*Castellari et al*., 2000]. This deep convection rate is an equivalent annual volume flux. Several approaches have been employed to estimate deep convection, which all rely on a specific property of the dense water formed. Table 1 summarizes the main DWF rate estimates in the NWMed from observations and numerical simulations.

Estimates of the mixed patch volume are based on the computation of a convective mixed layer depth (MLD) with either hydrological [*D'Ortenzio et al*., 2005] or dynamical [*Somot et al*., 2006] criteria. Then, all convective mixed layer volumes are integrated. From observations during winter 1991–1992, *Marshall and Schott* [1999] gave an order estimate of 0.3 Sv (with 1 Sv $= 10^6$ m^3/s), and several numerical simulations found a range of 0.01–1.62 Sv for periods between 1961 and 2007 [*Béranger et al*., 2010; *Herrmann et al*., 2009, 2010].

Several deep convection estimates rely on surface ocean properties which are well-observed by satellite. DWF leads to a vertical mixing of Chl_A that is otherwise located near the surface, which decreases its concentration at the surface. *Durrieu de Madron et al*. [2013] provided from observations an estimate of DWF rate of 1.1 Sv for winter 2012 from surface $[Chl_A]$ retrieval from satellite and assuming a constant MLD in the mixed patch. In addition, intense DWF is usually associated with a cyclonic gyre intensification and

Table 1. DWF Rate Estimates in the Northwestern Mediterranean Basin in Sv (1 Sv$=10^6$m^3/s) From Observations and Numerical Simulations[a]

Period	Estimates From Observations
Climatological mean	1.56 Sv *Bethoux* [1980], salinity budgets
	1 Sv *Tziperman and Speer* [1994], surf. diapycnal mixing (29 kg/m^3)
1991–1992	1.22 Sv *Rhein* [1995], box biogeochemical model inversion
	0.3 Sv *Marshall and Schott* [1999], mixed patch estimate
2004–2006 average	1.2 Sv *Schroeder et al*. [2008b], quantitative (θ, S) diagram
2011–2012	1.1 Sv *Durrieu de Madron et al*. [2013], satellite ocean color data
2012–2013	1.4 ± 0.3 Sv or 2.3 ± 0.5 Sv (this study), diapycnal mixing (29.11 kg/m^3)
2013 (restrat.)	-0.8 ± 0.4 Sv (this study), diapycnal mixing (29.11 kg/m^3)
	Estimates From Numerical Simulations
1958–2001	1.08 Sv average *L'Hévéder et al*. [2013a], diapycnal mixing in the ML
1958–1968	0.2–4 Sv *Naranjo et al*. [2014], diapycnal mixing (29.1 kg/m^3)
1960–1980	0.93 Sv *Somot et al*. [2006], diapycnal mixing (28.91 kg/m^3)
1961–2006	0.07–1.62 Sv *Herrmann et al*. [2010], mixed patch estimate
1979–2013	0.28 Sv average Somot et al. [2016], diapycnal mixing (29.10 kg/m^3)
1980–1988	0.2–1.6 Sv *Castellari et al*. [2000], diapycnal mixing in the ML
1986–1987	1.3 or 1.8 Sv *Herrmann et al*. [2008a], diapycnal mixing (29.1 kg/m^3)
1987–2007	0.9 Sv average *Pinardi et al*. [2013], diapycnal mixing in the ML
1988–2003	1.3 or 0.01–0.18 Sv *Béranger et al*. [2010], mixed patch estimate
1999–2007	0–1.28 Sv *Herrmann et al*. [2009], mixed patch estimate
2004–2006	1.73 Sv average *Beuvier et al*. [2012], diapycnal mixing (29.1 kg/m^3)
2012–2013	1.6 Sv Estournel et al. [2016], diapycnal mixing (29.11 kg/m^3)

[a]The period and methodology of computation is given in all cases. Note that estimates originally given in m^3 were converted into Sv by dividing by the number of seconds in 1 year, for comparison purposes.

therefore a negative sea level anomaly (SLA) in the convective region. Herrmann et al. (Long term interannual monitoring of open-ocean deep convection using altimetry and ocean color multi-sensors satellite data: Case study of the northwestern mediterranean sea, *Journal of Geophysical Research: Oceans*, submitted manuscript) deduced from a physical-biogeochemical model a relation between DWF and $[Chl_A]$-SLA anomalies and estimated a winter 2013 DWF rate between 1.5 and 2 Sv.

The evolution of the dense water hydrology can also be used to quantify the rate of dense water transformation by deep convection. Several studies are based on dense water salinity [*Bethoux*, 1980] or heat [*Walin*, 1982] budgets and others quantify transformations in the (θ, S) coordinates [*Walin*, 1982; *Schroeder et al*., 2008b; *Groeskamp et al*., 2014a,2014b]. *Bethoux* [1980] estimated the Western Mediterranean basin salinity budgets and deduced that the WMDW was formed by the mixing of 27% of surface water at a rate of 0.43 Sv and 73% of intermediate waters at a rate of 1.13 Sv, making up a total DWF rate of 1.56 Sv. *Schroeder et al*. [2008b] estimated an average annual DWF rate between 2004 and 2006 of 1.2 Sv from observed quantitative (θ, S) diagrams.

Other studies quantify density variations, also called diapycnal mixing, either at the surface [*Tziperman and Speer*, 1994], within the mixed layer [*Lascaratos*, 1993; *Castellari et al*., 2000; *Pinardi et al*., 2013] or at all depths [*Somot et al*., 2006; *Herrmann et al*., 2008a; *Beuvier et al*., 2012; *Naranjo et al*., 2014; *Estournel et al*., 2016]. *Tziperman and Speer* [1994] used climatological surface buoyancy fluxes and densities to deduce from the surface diapycnal mixing an upper bound of climatological DWF of 1 Sv in the NWMed Sea. Several modeling studies quantified diapycnal mixing in the mixed layer and found in periods between 1980 and 2007 average DWF rates between 0.2 and 1.6 Sv [*Castellari et al*., 2000; *Pinardi et al*., 2013], and others integrated diapycnal mixing at all depths and found in periods between 1958 and 2013 rates between 0.2 and 4 Sv [*Somot et al*., 2006; *Herrmann et al*., 2008a; *Beuvier et al*., 2012; *L'Hévéder et al*., 2013a; *Naranjo et al*., 2014; *Estournel et al*., 2016, *Somot et al*., 2016].

Note finally the possibility to quantify deep convection with specific ocean properties such as chlorofluoromethane and tritium concentrations [*Rhein*, 1995] found 1.22 Sv for winter 1991–1992), pO_2 anomaly at depth or a cold θ anomaly at intermediate depth as proxies of ventilated deep waters or intermediate waters that have been eroded by DWF.

The differences in results are not only due to the different methodologies and the large interannual variability of this phenomenon, both in observations [*Mertens and Schott*, 1998] and state-of-the-art models [*Somot et al*., 2006; *Herrmann et al*., 2010; *L'Hévéder et al*., 2013a], but also to the large uncertainty in observed DWF estimates and in the representation of DWF in models.

1.3. An Extensive Observation of the 2012–2013 Convective Year Over the NWMed

This study takes advantage of the exceptional measurement year of 2012–2013 in the NWMed Sea. Thanks to the MERMeX (Marine Ecosystems Response in the Mediterranean Experiment) [*Testor*, 2013; *Conan*, 2013] and HyMeX (Hydrological Cycle of the Mediterranean Experiment) programs, measurements have been carried out to study the impacts of DWF on the Mediterranean pelagic ecosystems Experiment (DeWex) in addition to those carried out on a long term basis in the framework of the Mediterranean Ocean Observing System for the Environment (MOOSE, http://www.moose-network.fr) [*Testor et al*., 2012, 2013]. In the framework of this long-term observatory, a large-scale observation cruise has been performed during summer 2012 and 2013. It will therefore be referred to in this study as the MOOSE network. In addition, during the DeWEx experiment, two cruises (DeWEx-1 and DeWEx-2) [*Testor*, 2013; *Conan*, 2013] using MOOSE network took place in winter and spring 2013. Those four cruises, referred as S12, W13, SP13, and S13, respectively, hereafter (standing for Summer 2012, Winter 2013, Spring 2013, and Summer 2013), give an estimate of the NWMed Sea dense water volume.

1.4. Oceanic OSSEs to Evaluate and Optimize Observing Systems

Several oceanic OSSEs have been employed to optimize existing or potential observing systems. *L'Hévéder et al*. [2013b] and *Alvarez and Mourre* [2014] focus on glider networks. The former estimate the optimal glider density to capture mesoscale variability, and the latter quantify the added value of glider coordination for the forecast of ocean temperature. *Hackert et al*. [1998] and *Ballabrera-Poy et al*. [2007] optimize mooring networks in order to minimize the error in the assimilated SSH and sea surface temperature (SST) fields.

Finally, *Mourre et al*. [2006] assess the potential performance of future satellite altimetry and tide gauge measurements to resolve high-frequency barotropic dynamics.

1.5. Aim of the Study

The aim of this study is to assess the accuracy of deep water volume estimates from MOOSE network via an OSSE and to quantify dense water volumes, DWF and restratification rates from observations in the period 2012–2013 including these error estimates. The OSSE therefore aims at quantifying comprehensively the observing system error, in contrast with previous oceanic OSSEs which aimed at optimizing it.

Section 2 describes OSSE methodology as well as the data and models used; section 3 presents the OSSE results; section 4 applies the results to estimate observed dense water variations in 2012–2013; section 5 discusses the methodology and potential applications of the OSSE; finally, section 6 summarizes the main results.

2. Methods, Models, and Data

The aim of this OSSE is to quantify the accuracy of dense water volume estimates by estimating MOOSE observing system errors. For that purpose, a numerical simulation is used as a virtual reality, virtual observations are carried out, the virtual observations are interpolated and finally the volume reconstruction error is quantified.

2.1. Creation of a Virtual Reality

This study uses as a virtual reality the free surface, generalized sigma vertical coordinate model SYMPHONIE, described by *Marsaleix et al*. [2009, 2012]. The model domain covers the entire convection area, with a 1 km horizontal resolution and a variable 40 level vertical resolution making of it an eddy-resolving ocean model. This model has previously been used in the Mediterranean to simulate convection in the open sea [*Herrmann et al*., 2008a; *Herrmann and Somot*, 2008] as well as coastal DWF [*Ulses et al*., 2008; *Estournel et al*., 2005; *Herrmann et al*., 2008b]. More recently, this model has been used to simulate the 2012–2013 convective year [*Estournel et al*., 2016]. The run used in this study is described by *Estournel et al.* [2016] who show a realistic initial state with regard to MOOSE large-scale observations and also a realistic simulation of ocean deep convection.

The dense water volume is deduced by integrating dense water thickness over space. Therefore, the virtual reality field is the bidimensional map of dense water thickness from SYMPHONIE. It is defined as the thickness of water which potential density ($z_{ref}=0$ db) exceeds 29.11 kg/m^3, which corresponds to maximal diapycnal mixing during the convective event in both observations (see section 4) and SYMPHONIE [*Estournel et al*., 2016]. A similar analysis is also done on density thresholds 29.08, 29.09, and 29.10 kg/m^3. Note that previous observational [*Tziperman and Speer*, 1994] and modeling [*Castellari et al*., 2000; *Herrmann et al*., 2008a; *Beuvier et al*., 2012; *Naranjo et al*., 2014; *Estournel et al*., 2016] studies used density levels from 28.91 to 29.11 kg/m^3 which corresponded to the respective levels of maximum diapycnal mixing.

Four periods are considered here which correspond to the ship cruises deployed over the NWMed: S12, W13, SP13, and S13. The central dates are resp. 1 August 2012, 12 February 2013, 13 April 2013, and 24 June 2013. For each period, we quantify MOOSE actual and theoretical networks' accuracy (see Figure 1, for the network maps), the former being used to evaluate the theoretical observing system and the latter to quantify uncertainties in observations. MOOSE actual networks include 68 (S13) to 82 (SP13) casts, whereas the theoretical network comprises 102 casts.

The analysis domain is a reduced NWMed region which covers most of the convective area: between [2.5°E; 9°E] and [40°N; 44°N], with a bathymetry $H > 2000$ m. Its volume is 3.28×10^{14} m^3. Figure 2 shows the annual dense water thickness variation range map for the period 1 August 2012 to 31 July 2013. Most areas with a thickness variation range exceeding 1500 m are included in the subdomain. They correspond to areas of DWF or where newly formed WMDW is advected. Therefore, despite large values along the northwestern shelf and southeast of Menorca, most dense water variations are captured by the domain and it allows for a compromise between the coverage of the DWF region and the availability of observations.

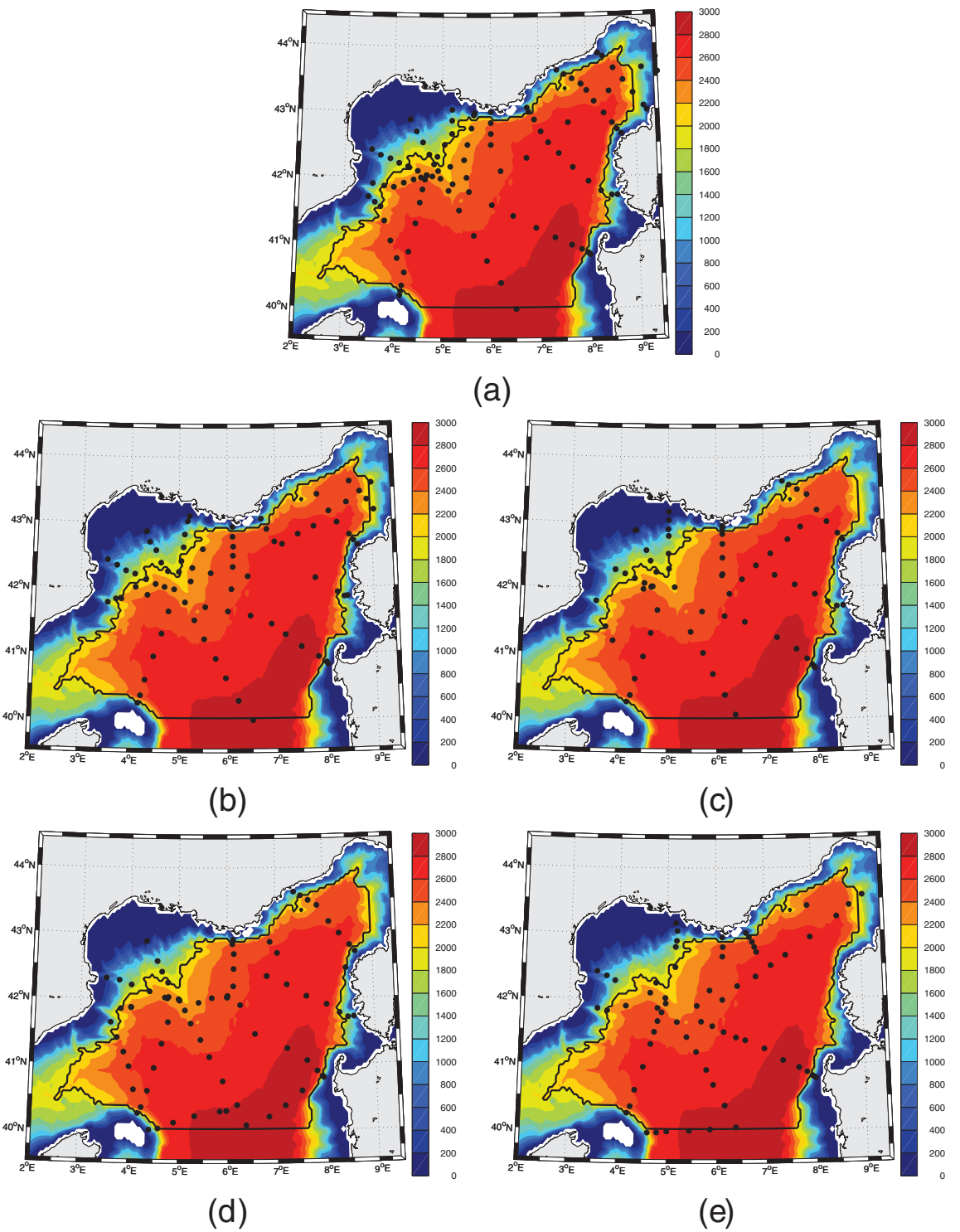

Figure 1. CTD casts locations for (a) MOOSE theoretical network and MOOSE actual networks during (b) S12, (c) W13, (d) SP13, and (e) S13 cruises. The black contour displays the analysis domain. The bathymetry is displayed in background of all figures.

2.2. Computation of Virtual Observations

We deal with all sources of error successively in order to quantify both their individual and cumulative impact on the total observing system error. First, space sampling error is assessed by generating 400 random networks of the same size as MOOSE network but with observation locations picked at random from a

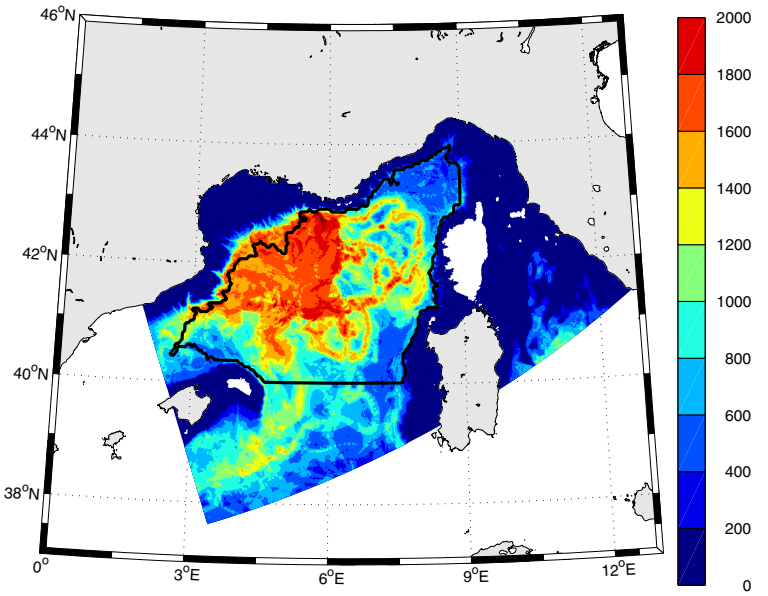

Figure 2. Map of simulated annual dense water thickness variation range (m), between 2 August 2012 and 31 July 2013. The black contour displays the analysis domain.

uniform distribution over the analysis domain. This ensemble size ensures a convergence of the error estimates (not shown). Virtual observations are picked at the central date of each period from the virtual reality field.

Second, the time coverage error is added by picking a random date for each virtual observation from all previously generated networks, from a uniform time distribution within each cruise period of 2–3 weeks.

Third, a Gaussian instrumental error is added to each virtual observation of the spatiotemporal network ensemble to account for the sensor accuracy. Finally, a systematic error, of Gaussian distribution among the network ensemble but constant for each network, is applied to account for instrumental stability. Whereas the instrumental accuracy is variable for each virtual observation, the instrumental stability is constant within a given network but variable between all networks. Both instrumental sources of error are based on W13 and SP13 cruises technical report [*Taillandier*, 2014], which estimates an instrumental accuracy of standard deviation (STD) 0.001 kg/m^3 and an instrumental stability of the order 0.001 kg/m^3. Errors on density measurements are converted into dense water thickness errors by estimating from all cruise data the average vertical density gradient at each isopycnal depth. The observed density gradient at the levels 29.08, 29.09, 29.10, and 29.11 kg/m^3 are 0.001 kg/m^3, respectively, every 5, 13, 50, and 125 m. The density error of 0.001 kg/m^3 is thus converted to a dense water thickness error of STD resp. 5, 13, 50, and 125 m for the density levels 29.08, 29.09, 29.10, and 29.11 kg/m^3, which is assumed to be Gaussian for both the instrumental accuracy and stability errors. Therefore, for the isopycnal 29.11 kg/m^3, the instrumental accuracy error is picked randomly for each virtual observation from a Gaussian distribution of $STD = 125$ m, and the instrumental stability error is picked randomly for each network, but constant within each network, from a Gaussian distribution of $STD = 125$ m.

2.3. Kriging of Virtual Observations

For each network, the dense water thickness is integrated over space on the analysis domain in order to deduce a dense water volume reconstruction. We perform a kriging of the virtual observations in order to reconstruct on the model grid the full bidimensional dense water thickness field. See Appendix A for a detailed description of the kriging method. This OSSE therefore does not include any assimilation procedure, contrary to *Mourre et al*. [2006], *Hackert et al*. [1998], *Ballabrera-Poy et al*. [2007], *L'Hévéder et al*. [2013b], and *Alvarez and Mourre* [2014]: indeed, the scientific aim is to provide a volume estimate independent from numerical models which can be later used for model evaluation purposes, and therefore to avoid the use of a model guess.

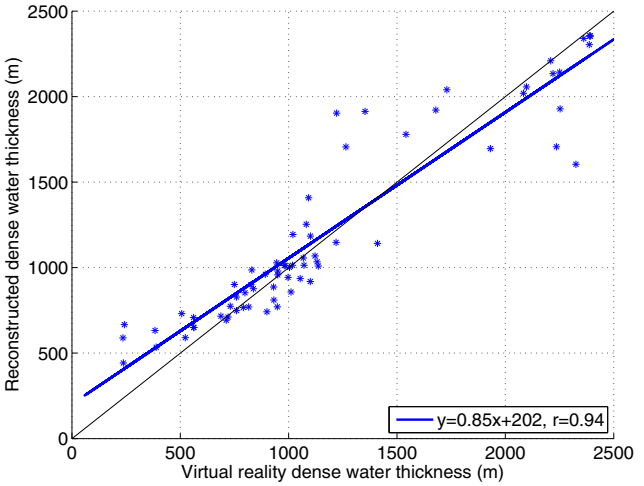

Figure 3. Scatterplot of reconstructed dense water thickness values at observation location as a function of dense water thickness actual value, in SYMPHONIE, for MOOSE theoretical network and the W13 ship cruise. The linear fit and correlation *r* are also given.

The interpolated field differs from the virtual reality even at virtual observations due to the fact that the kriging method retrieves the large-scale structures. Indeed, MOOSE network is not designed to sample mesoscale and smaller-scale structures which are of typical scale 15–50 km in the NWMed basin as its effective resolution is ≈ 50 km. Figure 3 displays the scatterplot of all reconstructed dense water thicknesses at observation locations with respect to virtual reality dense water thickness in SYMPHONIE for W13 period and MOOSE theoretical network. The linear fit shows an average absolute error of $|\epsilon| = 147$ m with a slope of 0.85. This means that the kriging method overestimates low values and underestimates high values, consistently with the large-scale reconstruction method which smoothes extreme values.

2.4. Assessment of the Reconstruction Error

Each random network provides a dense water volume reconstruction. The distribution of reconstruction error with respect to virtual reality gives access to an estimate of the 95% confidence interval in the volume estimate from observations, which will later be applied to actual observations. The root mean squared error (RMSE) deduced from the network ensemble is assumed to represent the STD of a Gaussian error variable. Therefore, the 95% confidence interval is given by $\pm 1.96RMSE$.

This framework provides four successive confidence intervals on volume estimates: a space error $\pm 1.96RMSE_s$, a spatiotemporal error $\pm 1.96RMSE_{st}$, a spatiotemporal and instrumental accuracy error $\pm 1.96RMSE_{sti1}$, and finally a spatiotemporal and full instrumental error $\pm 1.96RMSE_{sti2}$. The latter gives access to a global observing system error, whereas each one provides the successive contributions of each source of error.

In addition, for the space sampling ensemble, the space accuracy of the reconstructed dense water thickness map is addressed by computing its correlation *r* with the virtual reality field.

3. Results From Models

3.1. Modeled 2012–2013 Dense Water Thickness

Figure 4 shows the map of the simulated dense water thickness virtual reality, its reconstruction from MOOSE theoretical network and from MOOSE actual network during (a–c) S12, (d–f) W13, (g–i) SP13, and (j–l).

The model S12 field (Figure 4a) shows values between 1000 and 1400 m in the open-sea domain, with some mesoscale structures of higher or lower thickness most likely related to mesoscale eddies. Indeed, mesoscale eddies perturb the isopycnal levels by lifting (cyclonic) or lowering (anticyclonic) them. Only the eddies that extend vertically down to the 29.11 kg/m^3 isopycnal level, that is about 1000 m depth will have an impact on it. As a consequence, SCVs carrying lighter Levantine Intermediate Water (LIW) to the center of the NWMed domain do not impact the dense water thickness during S12 as the LIW extends approximately from 300 to 800 m depth [*Bosse et al.*, 2015]. The mesoscale structures observed in this period are related exclusively to the exchanges between the denser WMDW formed off the Gulf of Lions and lighter WMDW around them [*Demirov and Pinardi*, 2007]. Note that some unphysical patterns related to the initialization procedure might be visible for this period, as the S12 cruise is used to initialize SYMPHONIE and it therefore falls within the model spin-up phase. At the domain eastern and northern boundaries, the dense water thickness declines as a consequence of the incoming of lighter WMDW coming from the Algerian basin.

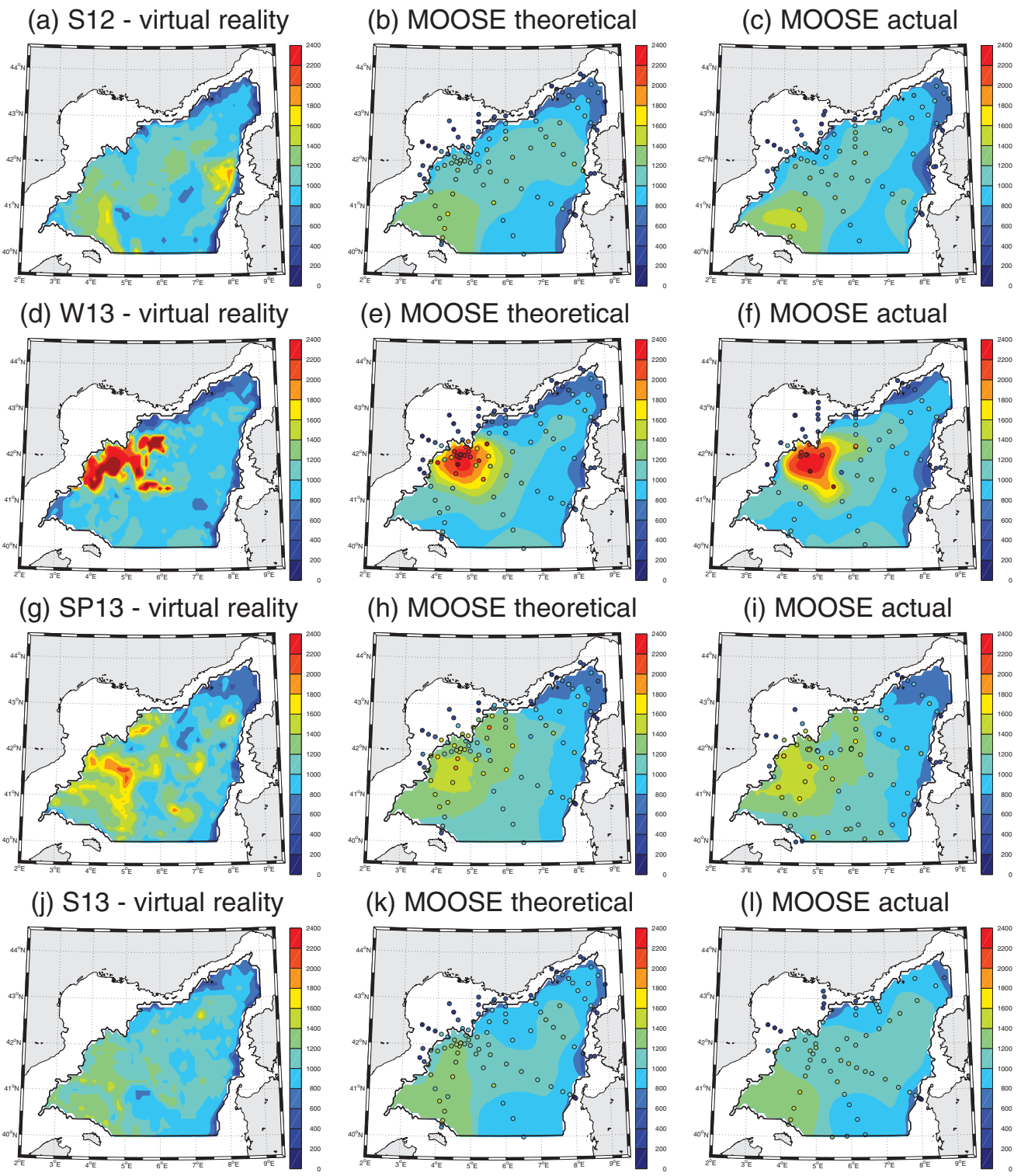

Figure 4. (a) Dense water thickness (m) virtual reality (SYMPHONIE) for S12 period; (b and c) Reconstructed field from MOOSE theoretical and actual networks (circles are the dense water thickness virtual observations from the network). Resp. (d–f), (g–i), and (j–l): same for W13, SP13, and S13 periods.

The W13 field (Figure 4d) shows a large increase off the Gulf of Lions, with thicknesses exceeding 2000 m that identify a mixed patch of newly formed dense waters extending over the whole water column. This patch tends to detach into a series of small-scale structures ($\approx$20$-$30 km size) that are mesoscale and sub-mesoscale eddies; on the other hand, eddies with lower dense water thickness enter the mixed patch [see

Herrmann et al., 2008a; *Estournel et al*., 2016]. They are both formed by baroclinic instability of the gyre rim current and contribute to restratification [*Madec et al*., 1991; *Marshall and Schott*, 1999]. The advection of lighter waters into the mixed patch area involves the first 1000 m of the water column as the dense water thickness is about 1000 m lower in those waters: therefore, the three main water masses of the NWMed are involved in this restratification process: the Atlantic Waters (AW) down to 300 m, the LIW from 300 to 800 m and the old WMDW below 800 m depth. In the other parts of the domain, the average dense water thickness decreases due to restratification between S12 and W13. Therefore, spatial gradients of dense water thickness are intensified both by convection in the mixed patch and restratification outside. This in turns activates dense water circulation [*Herrmann et al*., 2008a] by increasing the horizontal pressure gradient at depth.

The SP13 field (Figure 4g) shows several mesoscale structures of dense water thickness anomaly across the interior basin: the mesoscale eddies formed following the convective event are long-lived [*Testor and Gascard*, 2006], however they progressively mix up with the surrounding environment, and the dense water thickness field tends to homogenize. At the larger scale, a west-east dense water thickness gradient is forming between the newly formed dense water pole in the west and the old and lighter dense water in the east. It was already visible in previous observing [*Schroeder et al*., 2008a] and modeling [*Beuvier et al*., 2012] studies.

Finally, the S13 field (Figure 4j) is similar to S12: the small-scale variability has decreased as compared to SP13, although some mesoscale structures are still visible. The west-east basin-scale gradient is still visible but it is progressively replaced by the pattern of minimum dense water thickness at the eastern and northern boundaries already visible in S12 period.

Now looking at the reconstructed field from MOOSE theoretical network in Figures 4b, 4e, 4h, and 4k for illustration purpose, one notes a series of differences with the virtual reality. As large autocorrelation scales are used (see Appendix A, for more details), the kriging is not capable of reconstructing small-scale features as mesoscale eddies or strong gradients at the domain boundaries, which is consistent with a low-resolution observing network. Instead small-scale features are smoothed over large regions. However, the main large-scale features are visible: minimum values in the eastern and northern boundaries in S12 and S13 periods, a large-scale mixed patch of diameter $\approx$ 70 km during W13 and an east-west basin-scale gradient visible in SP13 and to a lesser extent in S13. The performance of the reconstructed field will be described below.

3.2. Space Sampling Error

We now consider the ensemble of 400 random space networks of same size as MOOSE theoretical network to quantify the observing error related to space sampling. Table 2 shows for MOOSE theoretical and actual networks and all ship cruises, the virtual reality dense water volume, the space 95% confidence interval (expressed in percent of the virtual reality volume) given by 1.96 $RMSE_s$ as well as the average space correlation of this ensemble r, the spatiotemporal confidence interval 1.96 $RMSE_{st}$, the spatiotemporal and instrumental accuracy confidence interval 1.96 $RMSE_{sti1}$ and finally the total observing system confidence interval 1.96 $RMSE_{sti2}$. The simulated dense water volume increases successively between S12 and W13 and between

Table 2. Dense Water Volume From Virtual Reality V, Space Confidence Interval 1.96 $RMSE_s$ and Correlation r, Spatiotemporal Confidence Interval 1.96 $RMSE_{st}$, Spatiotemporal and Instrumental Accuracy Confidence Interval 1.96 $RMSE_{sti1}$, and Total Observing System Confidence Interval 1.96$RMSE_{sti2}$, for all Cruise Periods and for Both MOOSE Theoretical and Actual Networks[a]

	Theoretical Network				Actual Networks			
	S12	W13	SP13	S13	S12	W13	SP13	S13
V (10^{13} m^3)	11.9	13.1	14.9	14.1	11.9	13.1	14.9	14.1
1.96 $RMSE_s$ (%)	4.1	6.7	4.4	3.0	4.6	8.3	4.8	4.1
r	0.69	0.75	0.73	0.73	0.65	0.71	0.71	0.68
1.96 $RMSE_{st}$ (%)	4.1	8.6	4.0	3.0	4.6	9.5	5.0	3.8
1.96 $RMSE_{sti1}$ (%)	4.8	8.8	4.4	3.8	5.5	10.0	5.7	4.9
1.96 $RMSE_{sti2}$ (%)	26.3	25.0	23.2	22.1	24.7	24.9	22.0	24.8

[a]The confidence interval is given at the 95% probability level, in percent of the virtual reality volume.

W13 and SP13 in SYMPHONIE, which confirms that DWF occurred both before and after W13 cruise in the simulation. It then decreases between SP13 and S13 as a result of restratification.

Now looking at the error and space correlation deduced from MOOSE theoretical network space ensemble, the confidence interval is between 3.0% and 6.7%. This relatively low error illustrates that MOOSE theoretical network density of observations is sufficient to estimate dense water volume in 2012–2013 with high confidence. It also suggests that the volume estimate is little sensitive to the spatial distribution of observations as the networks were constructed randomly. However, W13 period shows the highest error, which provides evidence that a higher observation density is necessary in this period. This is consistent with the space patterns of the dense water thickness in W13 (Figure 4d) with strong gradients between the mixed patch and the rest of the domain. However, despite a high accuracy in estimating the integrated volume, the space correlation of the reconstructed dense water thickness with the virtual reality is relatively low, between 0.69 and 0.75. This is due to the kriging method which only reconstructs the large-scale: despite large errors in the small-scale structures, the large-scale, and therefore the integral volume, are accurately reconstructed. The period with the lowest correlation is S12 and has more small-scale structures, whereas the period with the highest correlation is W13 and has more large-scale structures (see Appendix A, for more details).

As a conclusion, MOOSE theoretical network has a satisfactory observation density and space sampling is not crucial given the number of observations: it is fit to reconstruct the NWMed Sea dense water volumes. However, small-scale features are not captured by this network which leads to larger error in the bidimensional reconstruction of the dense water thickness.

3.3. Spatiotemporal Sampling Error

We now turn to the confidence interval deduced from the spatiotemporal sampling ensemble shown in Table 2. The 95% confidence interval 1.96 $RMSE_{st}$ is comprised between 3.0% and 8.6%, which is relatively low. Only in W13 period, it is higher than the space-only confidence interval. This means that in most cases, the time sampling error does not add to the space sampling error. In SP13 period, it has even decreased as compared to the space-only error: this might be related to a lower space dispersion in average during the SP13 period as compared to the central date. However, W13 shows a clear error increase that can be attributed to the time variability of dense water volumes during W13.

As a consequence, the time sampling error only adds marginally to the space sampling error, and the total sampling error of MOOSE theoretical network is low. This means that the ship cruises are rapid enough to measure accurately dense water volumes.

3.4. Sampling and Instrumental Accuracy Error

We now consider the confidence interval deduced from the sampling and instrumental accuracy ensemble shown in Table 2. The 95% confidence interval 1.96 $RMSE_{sti1}$ is comprised between 3.8% and 8.8%, which remains relatively low. In all cases, adding instrumental accuracy error has only marginally increased the total error, between 0.2% and 0.7%. However, for a given virtual dense water thickness observation, a Gaussian perturbation of $STD = 125$ m has been applied, which is more than a 10% perturbation in most of the analysis domain. The low impact in the reconstructed volume error can be explained by an average error compensation over each virtual network as this perturbation is null in average.

As a consequence, the observing system instrumental accuracy is largely sufficient to estimate accurately dense water volumes.

3.5. Full Sampling and Instrumental Error

We finally consider the total observing system error, once the instrumental stability error has been added to the previous ones, shown in Table 2. The 95% confidence interval 1.96 $RMSE_{sti2}$ is comprised between 22.1% and 26.3%, which is larger by a factor 2.8–5.8 than the previous error estimate. As a conclusion, the instrumental stability error largely dominates the total observing system error. This is due to the fact that the stability error uplifts or lowers the isopycnal depth at the basin-scale. In addition, the low potential density vertical gradient at depth leads to potential large errors in the isopycnal level depth.

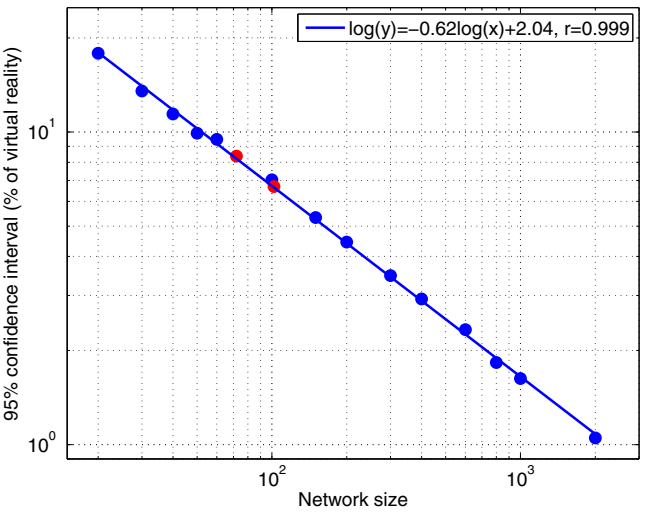

Figure 5. Space sampling 95% confidence interval (in % of virtual reality) as a function of the network size (from 20 to 2000 observations per network) for W13 period; red dots represent, respectively, MOOSE actual size for W13 cruise (72 points) and theoretical size (102 points). The line represents the logarithmic fit, its formula and correlation are given.

Note that the observations used in this study have been thoroughly post-treated and intercalibrated in order to ensure instrumental error tends to be null. Both error estimates including instrumental error are therefore an upper bound of the expected actual instrumental error.

3.6. How Does the Network Size Impact Space Error?

In this section, we try to characterize the evolution of space error with the network size. For that purpose, for the W13 period, the same space error estimate is done with 400 member ensembles of networks of size varying from 20 to 2000 observations. The ensemble 95% confidence interval $1.96\,RMSE_s$ is given as a function of the network size in Figure 5 in a logarithmic scale, including also MOOSE actual W13 network (72 casts) and theoretical (102 casts) network sizes. The error is indeed a strictly decreasing function of network size, following remarkably well a power law of parameter $\alpha = -0.62$ ($r > 0.99$). MOOSE actual and theoretical networks, represented with red dots in Figure 5, fit closely the logarithmic regression. The 95% confidence interval ranges from 19% for a 20 point network to 1% for a 2000 point network. This means that any doubling of network size will lead to an error decrease by 35%.

As a consequence, even with a 20 point network, the space confidence interval would remain lower than the total confidence interval of MOOSE theoretical network, which is dominated by the instrumental stability error. In addition, a 50 point network would be sufficient to obtain a space confidence interval lower than 10%. This confirms that MOOSE network density is largely sufficient to estimate accurately dense water volumes. Potential observing systems can be dimensioned using an accuracy threshold from this relation.

4. Observed 2012–2013 Dense Water Volume Evolution

Using the methodological framework described above, the dense water volume evolution is quantified together with its confidence interval from observations in the 2012–2013 period.

4.1. Evolution of the Dense Water Thickness Over the Basin

We first focus on the spatial structure of dense water evolution in the 2012–2013 period. Figure 6 displays the observed dense water thickness computed at the 29.11 kg/m^3 level and its bidimensional reconstruction for all cruise periods. The dense water evolution between S12 and SP13 and between SP13 and S13 is also displayed. During S12 cruise, the observed dense water thickness shows a maximum value in the southwest of the basin and minimal values both in the Ligurian Sea and north of the basin. Both patterns resemble those of SYMPHONIE simulation and they might be associated with the exiting of a previous WMDW to the southwest of the basin [*Béthoux et al*., 2002; *Beuvier et al*., 2012], balanced by an incoming of old and lighter WMDW from the Algerian basin and the Ligurian Sea through a cyclonic deep boundary current [*Demirov and Pinardi*, 2007].

The pattern of dense water thickness is very different during W13 period, with two compensating trends. On the one hand, dense water increases sharply in the mixed patch, associated with the formation of new WMDW. There is no clear dense water increase in the Ligurian Sea, suggesting that ocean convection was not deep and dense enough to reach the 29.11 kg/m^3 density level in this basin. On the other hand, all regions outside of the mixed patch and Ligurian Sea show a clear decrease between S12 and W13,

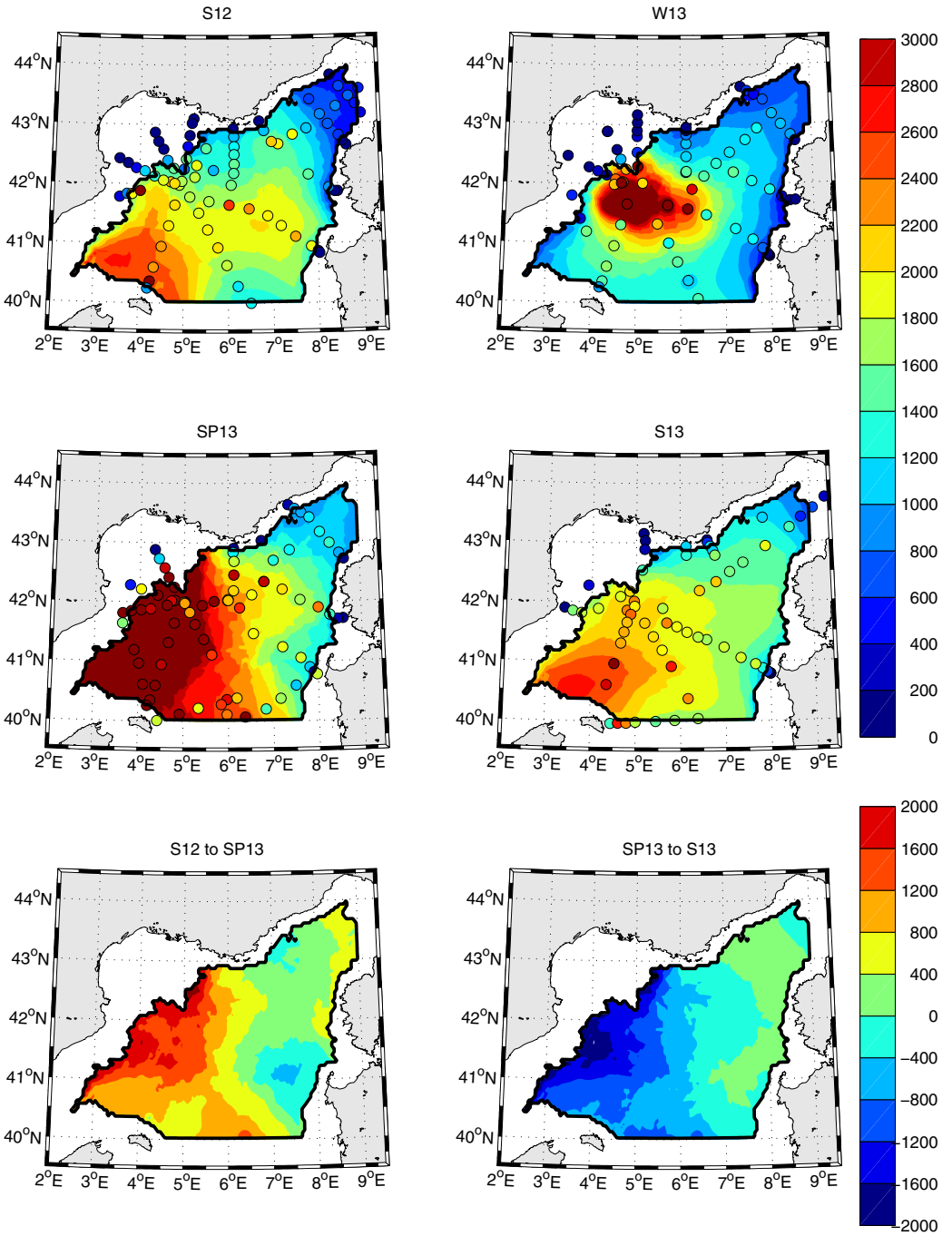

Figure 6. (top and middle plots) Dense water thickness map (m) reconstructed from observations (dots) at the level 29.11 kg/m^3 and for each period. (bottom plots) Dense water thickness variation map (m) reconstructed from observations between S12 and SP13, and between SP13 and S13.

suggesting a continued restratification. As a result, it is not clear that between S12 and W13, DWF dominates over restratification.

On the contrary, the observed dense water thickness during SP13 is in average higher over almost all the domain than during S12 and W13 periods. This period closely follows the end of the DWF event and a large increase of dense water volume is visible west of 6.5°E. This newly formed dense water was produced either locally in the mixed patch area, or it was advected from it to the southwest of the basin, a pattern that was already visible in SYMPHONIE (Figure 4g) during SP13 and in observations during S12 period. Thick columns

of convective waters ($H > 2500$ m) have already reached the south of the analysis domain and are likely to be advected to the Algerian basin [*Beuvier et al*., 2012; *Demirov and Pinardi*, 2007]. In the eastern half of the domain, the 29.11 kg/m^3 isopycnal level has been lifted and as a consequence the dense water thickness is also increased, although less than in the west. This might result from both advection and mixing of newly formed WMDW [*Béthoux et al*., 2002]. The period between S12 and SP13 thus seems to be the most adequate to estimate DWF. Indeed, during W13, most of the dense waters are not formed yet and the observing system error is higher.

Finally, during S13, the observed dense water thickness resembles highly that of the S12 period, although it is slightly higher in average. The dense water thickness has dramatically decreased west of 6.5°E as compared to SP13, and high values ($H > 2000$ m) are only present in the southwest of the domain. The dense water thickness is lowest in the east and north of the domain, however it remains almost constant in those regions between SP13 and S13. As a consequence, the dense water decrease between SP13 and S13 can be used to estimate a restratification rate in that period.

The map of dense water thickness evolution between S12 and SP13 confirms a large volume increase, mostly from the western half of the basin. The average thickening for this area is higher than 1000 m. This area is generally south and west of the mixed patch area which could be identified from W13 period, suggesting that most of the export of new WMDW is oriented southwestward, in agreement with previous observing [*Schroeder et al*., 2008a] and modeling [*Demirov and Pinardi*, 2007; *Beuvier et al*., 2012] results. Once again, between SP13 and S13 periods, most of the dense water evolution occurs west of 6.5°E, with an average dense water shallowing slightly lower than 1000 m. This suggests that a large fraction of the dense water formed in the winter 2013 is in late June either destroyed by internal mixing or advected southwestward outside of the NWMed basin.

4.2. Dense Water Volume Estimates

The volume of waters denser than 29.11 kg/m^3 is estimated from observed CTD casts with the reconstruction method presented in section 2, and the 95% confidence interval is deduced from the same OSSE applied on the actual MOOSE networks. The dense water thickness reconstruction from the actual networks (Figures 4c, 4f, 4i, and 4l) is very similar to that with the theoretical network, even if the reconstruction is degraded due to the fewer observations. Table 2 provides the 95% confidence interval related to the four sources of observation error as well as the space ensemble average correlation with virtual reality. Space error given by 1.96 $RMSE_s$ is only little increased with respect to the theoretical network, with low values comprised between 4.1% and 8.3% and with a space correlation slightly decreased to 0.69 in average. Spatiotemporal error given by 1.96 $RMSE_{st}$ also increases little, between 3.8% and 9.5%. The same is true for the spatiotemporal and instrumental accuracy error given by 1.96 $RMSE_{sti1}$ with values between 4.9% and 10.0%. Finally, the total error given by 1.96 $RMSE_{sti2}$ remains highly dominated by the instrumental stability error and therefore it is comparable between MOOSE theoretical and actual networks.

As a consequence, for the observed volume estimate, two confidence intervals are displayed: a sampling confidence interval given by 1.96 $RMSE_{st}$ which is below 10% in all cases, and a total confidence interval dominated by the instrumental stability error and comprised between 22.0% and 24.9%. Indeed, the observations used in this study have been thoroughly intercalibrated and therefore the latter confidence interval is likely to overestimate the actual observation error. In addition, a high instrumental error would imply a homogeneous uplift or lowering of the dense water thickness over the whole domain, which is not what is observed from Figure 6. This gives further confidence in a low instrumental error and an observing system error well approximated by the sampling error only.

Table 3 compiles the observed dense water volume estimates with their 95% confidence interval, for densities between 29.08 and 29.11 kg/m^3, and only the volume estimates for the 29.11 kg/m^3 level since such densities are not represented in SYMPHONIE simulation. The volume of waters denser than 29.11 kg/m^3 shows that the period between S12 and W13 was associated with a slight increase in the estimated dense water volume, from 13.3 to 13.7 $\times$ 10^{13} m^3. However, this volume increase of 0.4 $\times$ 10^{13} m^3 is not significant which certainly reflects a compensation between restratification and start of deep convection as suggested by *Visbeck et al*. [1996]. Moreover, the DWF process was still active after the W13 period and this explains why the SP13 cruise shows significantly higher volumes of dense water, reaching 17.7 $\times$ 10^{13} m^3 ($p > 0.95$, assuming both volume estimates are independent). Finally, dense water volume decreases

Table 3. Observed Dense Water Volume Estimates (10^{13} m^3) for All Ship Cruises and Density Levels Between 29.08 and 29.11 kg/m^3 With Its 95% Confidence Interval[a]

σ_0 (kg/m^3)	S12 1 August 2012 79 CTDs	W13 12 February 2013 72 CTDs	SP13 13 April 2013 82 CTDs	S13 24 June 2013 68 CTDs
29.08	28.3 ± 0.7 (±0.7)	30.0 ± 1.0 (±1.0)	30.3 ± 0.7 (±0.7)	30.1 ± 0.8 (±0.8)
29.09	27.5 ± 0.7 (±0.8)	29.1 ± 1.1 (±1.2)	29.6 ± 0.7 (±0.7)	29.4 ± 0.8 (±0.9)
29.10	25.3 ± 0.7 (±1.4)	26.3 ± 1.4 (±2.0)	28.1 ± 0.8 (±1.7)	27.3 ± 0.9 (±1.9)
29.11	13.3 ± 0.6 (±3.3)	13.7 ± 1.3 (±3.4)	17.7 ± 0.9 (±3.9)	15.1 ± 0.6 (±3.8)
29.12	2.0	0.7	2.5	1.0

[a]The first confidence interval includes only spatiotemporal sampling errors and corresponds to 1.96 $RMSE_{st}$, whereas the second (in brackets) includes also instrumental errors and corresponds to 1.96 $RMSE_{sti2}$. At the level 29.12 kg/m^3, only the volume estimates are provided as this density class is not simulated by SYMPHONIE.

significantly ($p > 0.95$) between SP13 and S13 periods and it reaches 15.1 × 10^{13} m^3 as a result of the restratification phase. Note that the S13 dense water volume is higher than during S12. It can be related to the very intense 2012–2013 DWF event that induces a densification of the whole basin that does not fade away on the seasonal scale. To a lesser extent, it could also be related to the earlier date of the S13 cruise (24 June) with respect to S12 cruise (1 August). Note however that none of these volume evolutions is significant when including the instrumental error: this illustrates the sensitivity of results to instrumental stability, although it can be reasonably assumed that instrumental stability was low in the observations considered here.

In this study, the 2012–2013 DWF rate is estimated from the volume evolution between S12 and SP13 cruises to avoid the transient effect and larger error of the volume estimate during W13 cruise, and the restratification rate is estimated between SP13 and S13 periods. Assuming both volume estimates are independent, the squared errors computed in the OSSE can be added in order to deduce a volume variation error for both periods. The DWF and restratification rates and their relative errors are shown in Table 4 for density levels 29.08–29.11 kg/m^3, and only the transformation rates are given for the level 29.12 kg/m^3. For the level 29.11 kg/m^3, the relative errors on the volume variation are higher than on the actual volume, reaching 24% for the DWF rate and 42% for the restratification rate, as compared to less than 10% for the actual volume. This is due partly to the absolute error increase and mostly to the lower values of volume variations as compared to the actual volumes. The DWF rate is estimated at 4.5 × 10^{13} m^3, largely significant when assuming a null instrumental error. It can be converted into an equivalent annual flux of 1.4±0.3 Sv, which is in the upper end among previous DWF rate estimates in the NWMed (see Table 1, for a comparison). The restratification rate is estimated at −2.6 × 10^{13}m^3 or equivalently −0.8±0.3 Sv, which is also largely significant assuming a low instrumental error. This is, to our knowledge, the first restratification rate estimate from observations in the NWMed basin.

Finally, the same computations for other density levels confirm that the diapycnal mixing rate is maximum for waters denser than 29.11 kg/m^3 during both periods. This means that in the 2012–2013 period, the 29.11 kg/m^3 level captures best the deep ocean ventilation. The DWF rates are resp. of 0.6±0.3, 0.7±0.3, 0.9±0.4, and 0.2 Sv for density levels of 29.08, 29.09, 29.10, and 29.12 kg/m^3. The restratification rates are resp. of −0.1±0.3, −0.1±0.3, −0.3±0.4, and −0.5 Sv for the same levels. We note that the instrumental error decreases sharply when density decreases, which is due to the increase of the vertical density gradient when density decreases.

Table 4. Observed DWF and Restratification Rates for Density Levels Between 29.08 and 29.11 kg/m^3 With Its 95% Confidence Interval[a]

σ_0 (kg/m^3)	DWF Rate (S12–SP13)	Restratification Rate (SP13 to S13)
29.08	2.0 ± 1.0 (±1.0) × 10^{13} m^3 0.6 ± 0.3 (±0.3) Sv	−0.2 ± 1.0 (±1.0) × 10^{13} m^3 −0.1 ± 0.3 (±0.3) Sv
29.09	2.1 ± 1.0 (±1.1) × 10^{13} m^3 0.7 ± 0.3 (±0.3) Sv	−0.3 ± 1.0 (±1.1) × 10^{13} m^3 −0.1 ± 0.3 (±0.4) Sv
29.10	2.8 ± 1.1 (±2.2) × 10^{13} m^3 0.9 ± 0.4 (±0.7) Sv	−0.8 ± 1.2 (±2.4) × 10^{13} m^3 −0.3 ± 0.4 (±0.7) Sv
29.11	4.5 ± 1.1 (±5.1) × 10^{13} m^3 1.4 ± 0.3 (±1.6) Sv	−2.6 ± 1.1 (±5.3) × 10^{13} m^3 −0.8 ± 0.3 (±1.7) Sv
29.12	0.5 × 10^{13} m^3 0.2 Sv	−1.5 × 10^{13} m^3 −0.5 Sv

[a]The first confidence interval includes only spatiotemporal sampling errors and corresponds to 1.96 $RMSE_{st}$, whereas the second includes also instrumental errors and corresponds to 1.96 $RMSE_{sti2}$. At the level 29.12 kg/m^3, only the volume estimates are provided as this density class is not simulated by SYMPHONIE.

Computing DWF rate in the reduced analysis domain and between S12 and SP13 is not equivalent as computing the actual DWF rate over the whole NWMed domain and between the

beginning and the end of the DWF event. SYMPHONIE simulation is used to extrapolate the results over the whole NWMed domain and between the dates of annual minimum and maximum dense water volume. In SYMPHONIE, the DWF rate is higher by 63% when computing it over the whole domain and between the dates of minimum and maximum dense water volume, due to 1/3 to the reduced analysis domain and to 2/3 to the observation dates. This factor applied to observations gives a total DWF estimate of $7.3 \pm 1.8 \times 10^{13} m^3$ or equivalently 2.3 ± 0.5 Sv. This is the largest DWF rate observed in the NWMed basin, which suggests the 2012–2013 DWF event was exceptional. This also suggests that the optimal cruise dates to measure the winter 2013 DWF rate from the dense water volume evolution would have been mid-January, before the beginning of DWF (long after S12 cruise), and late-March, after its end (close to SP13 cruise).

4.3. Dense Water Evolution as a Function of Density

Dense water volume transformations result from surface formation by atmospheric fluxes, diapycnal mixing, and lateral advection through the boundaries of the NWMed domain [*Somot et al.*, 2006]. A volume integration for different density levels allows to identify which water masses are formed and disappear during the different phases of the 2012–2013 convective event.

Figure 7 shows the diapycnal mixing rate as a function of density, that is the volume formation of denser waters, from S12 to SP13, SP13 to S13 and for the whole S12 to S13 period. Its derivative with respect to density allows to identify which density classes are formed and disappear. A positive (resp. negative) derivative indicates that more water exits (resp. enters) than enters (resp. exits) a density class and as a result, the density class is reduced (resp. formed) at a rate given by the rate of entrance minus the rate of exiting in this water class [see *Somot et al.*, 2006, for more details on the methodology].

The DWF rate between S12 and SP13 (blue curve) is indeed maximal at the 29.11 kg/m^3 threshold and is null for waters denser than 29.125 kg/m^3. This means that the new dense waters have mainly a density between 29.11 and 29.125 kg/m^3 and form at an annual rate of 1.4 Sv. 3/4 of the new dense waters have a density between 29.115 and 29.12 kg/m^3. By volume conservation, this dense water results from the destruction of lighter waters. The DWF rate curve reveals that half of it has a density comprised between 29.08 and 29.11 kg/m^3, whereas the second half is lighter than 29.08 kg/m^3 by conservation (not shown in the figure). This corresponds, respectively, to half of LIW and old WMDW, and half of AW being transformed into new WMDW waters at a rate of $\approx$ 0.7 Sv each.

The restratification rate between SP13 and S13 shows a partly symmetric picture of water class transformation: whereas waters lighter than 29.11 kg/m^3 are formed at a rate of 0.8 Sv, the same amount of denser waters disappears. More specifically, 90% of the water formed has a density of $29.09 < \sigma_0 < 29.11\,kg/m^3$, which is characteristic of lighter WMDW, and all the waters that disappear have a density of $29.11 < \sigma_0 < 29.125\,kg/m^3$: the restratification phase seems to consume the densest waters and to produce mostly lighter WMDW.

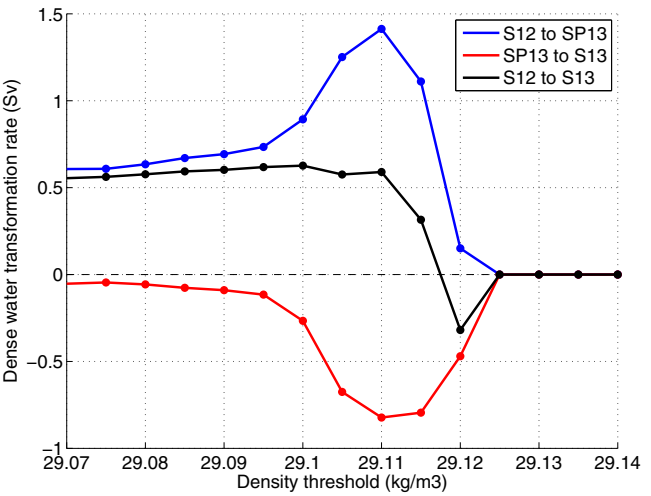

Figure 7. Blue dots: DWF rate (Sv) estimated between S12 and SP13 cruises as a function of density. Red dots: same for the restratification rate estimate between SP13 and S13 cruises. Black dots: sum of DWF and restratification rates given by the dense water variation rate between S12 and S13 cruises.

Finally, the volume variations in the S12–S13 period are associated with an annual volume formation of 0.9 Sv for waters having a density of $29.1 < \sigma_0 < 29.12\,kg/m^3$, a water destruction at a rate of 0.3 Sv at the highest density ($\sigma_0 > 29.12$) and a water destruction at a rate of 0.6 Sv, mostly at densities lower than 29.07 kg/m^3. Therefore, there seems to be an annual dense water accumulation in the basin,

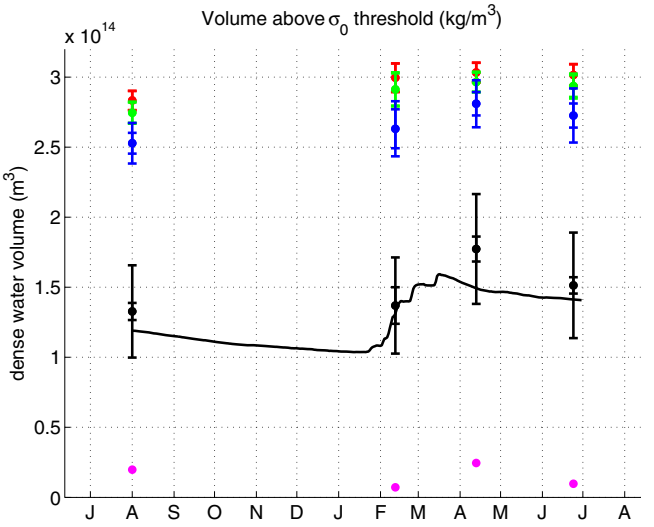

Figure 8. Error bars: estimated dense water volume and their 95% confidence interval in observations for all cruises and for (red) 29.08 kg/m^3, (green) 29.09 kg/m^3, (blue) 29.10 kg/m^3, and (black) 29.11 kg/m^3 density thresholds. The small error bar includes only spatiotemporal sampling errors and corresponds to 1.96 $RMSE_{st}$; the large one includes also instrumental errors and corresponds to 1.96 $RMSE_{sti2}$. Pink dots correspond to the dense water volume estimate at the 29.12 kg/m^3 level. The black curve displays the simulated daily time series of dense water volume at 29.11 kg/m^3 in SYMPHONIE.

due at 2/3 to the transformation of LIW and AW into dense waters, and at 1/3 to the disappearance of the densest waters. The first transformation suggests an annual trend of dense waters due to the large 2012–2013 DWF event. However, part of this annual difference might also be related to the delay between S12 cruise on 1 August and S13 on 24 June. This hypothesis is weakened by the fact that the restratification rate given by SYMPHONIE simulation from 24 June 2013 to 1 August 2013 is only $-0.15Sv$, which is far lower than the annual volume transformation of 0.6 Sv shown in Figure 7.

The destruction of the densest water class in this period is more challenging to interpret: a former study [*Durrieu de Madron et al.*, 2013] has revealed that the 2011–2012 convective event in the NWMed was marked with a large fraction of DWF by cascading, forming a denser layer at the bottom of the water column, with a cold and fresh signature. Such water masses might have disappeared over the year due to less intense cascading in the 2012–2013 winter, interior mixing or advection outside of the domain.

4.4. Model Validation at the 29.11 kg/m^3 Density Threshold

The dense water volume has been estimated in observations with a confidence interval accounting for sampling and instrumental error. The simulation used in this study can now be evaluated a posteriori in terms of its capacity to reproduce dense water volume variations in 2012–2013. Figure 8 represents the daily variations of dense water volume in SYMPHONIE simulation at the 29.11 kg/m^3 level, as well as the 95% confidence interval from observation including the sampling and total error. In addition, observed volumes are given from observations in the levels 29.08, 29.09, 29.10, and 29.11 kg/m^3.

SYMPHONIE observed S12 volume is in relative agreement with observations, although it is slightly underestimated. In the W13 period, there is a good agreement between observations and SYMPHONIE simulation. In the simulation, the volume reaches its minimum in late January, just before the violent mixing phase of the deep convection, and it its maximum in mid-March. The volume in the SP13 period is underestimated in SYMPHONIE simulation, which leads to an underestimate of the DWF rate by this simulation. The difference is significant only when excluding the instrumental error, however as argued before a low instrumental error is expected from the observations used in this study. Finally, the S13 dense water volume has a low negative bias in SYMPHONIE simulations, resulting from a partial compensation between too low DWF and restratification rates.

As a consequence, SYMPHONIE simulation has no significant bias ($p < 0.95$) when including all observation errors, but it has a significant ($p > 0.95$) negative bias in all but W13 periods when excluding instrumental error. However, the bias is lower than 10% in S12 and S13. The dense water volume is therefore well captured in most periods by this simulation and this supports our error estimates.

5. Discussions

5.1. Hypotheses of the OSSE

Each step of the OSSE implies some hypotheses. The main hypotheses are related to the selection of the virtual reality, to the random network ensemble construction and to the dense water reconstruction method. The numerical simulation used as a virtual reality is assumed to be accurate enough for results to be transposable

in observations. Modeled dense water volumes from SYMPHONIE simulation have been evaluated a posteriori with regard to observations in section 4 and they show low biases in all but SP13 period, which validates their use for this OSSE. Moreover, the same OSSE has been performed on an eddy-permitting (7 km resolution) ocean simulation with a similar initial state as SYMPHONIE and results (not shown) were very similar. This suggests that results are little sensitive to the model horizontal resolution in the 1–7 km resolution range.

The network ensemble reconstruction assumes that a random selection of measurement dates and locations from a uniform distribution gives the spatiotemporal error related to MOOSE network. However, MOOSE network is designed with both scientific and practical constraints and the dates and locations are not picked at random. An alternative option would have been to fix MOOSE network location and to use a dense water thickness field from different years, however the simulation was done only in the period 2012–2013. In addition, the space correlation of MOOSE network reconstruction with the virtual reality is comparable to the average space correlation of the random networks, which suggests that their performance in capturing the dense water volume is similar. As for the time sampling, it is a reasonable hypothesis that MOOSE network time distribution of sampling is homogeneous over the period, as the CTD casts are done at a regular frequency.

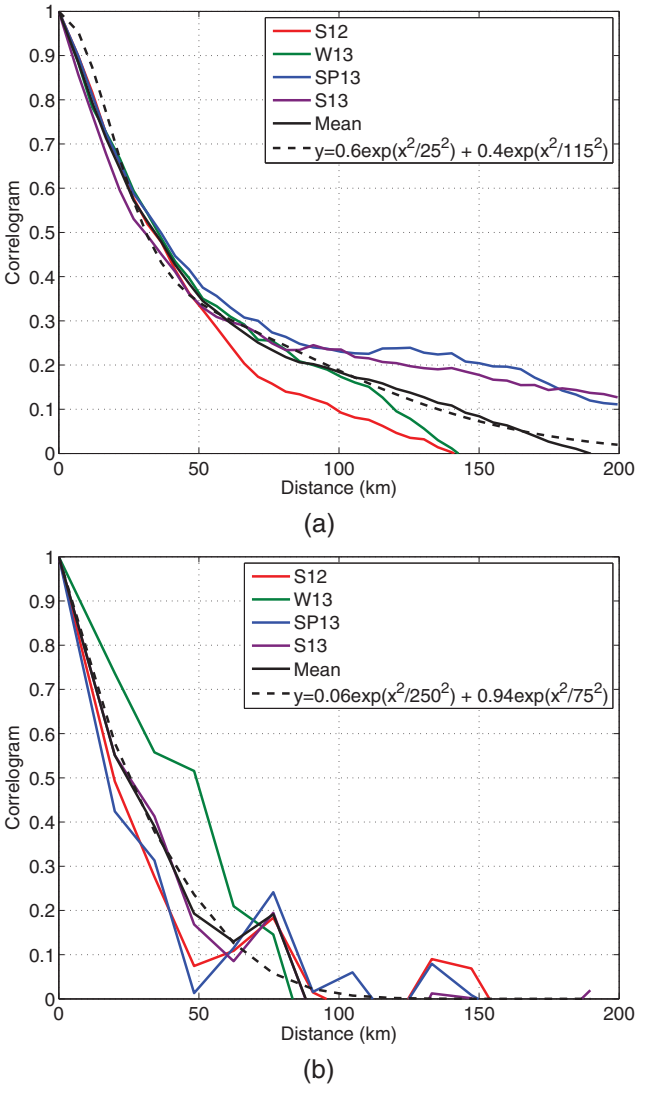

Figure 9. (a) Correlogram of simulated dense water thickness for each cruise and average (black line). The dashed line gives the least square fit for the mean correlogram with its formula. (b) Same as Figure 9a deduced from the subsampled field by MOOSE theoretical network.

Finally, the kriging method used to reconstruct the field implies a series of hypotheses. The choice of using no model guess to fill the field far from any observation leads to high errors at such locations. In this study, the dense water volume estimates are constructed as independent to model fields as possible, for model validation purposes. In addition, state-of-the-art ocean reanalyses in the Mediterranean Sea show high discrepancies in deep water hydrology (e.g., *Pinardi et al.*, 2013; *Hamon et al.*, 2016]. This makes their use as backgrounds for challenging for deep waters and they were not considered in this study. The space correlation scales selected in the kriging method also impact results, however they vary for each virtual network depending on the reconstructed correlogram (see Appendix A), therefore their associated error is implicitly accounted for in the random network ensemble.

5.2. Applying the OSSE to Other Variables

The same OSSE can be applied to other bidimensional physical variables sampled by MOOSE network. The specific results will however be variable-dependant.

In particular, the same methodology could be applied to estimate DWF rate from other physical or biogeochemical diagnostics. Note however a few drawbacks of alternative DWF rate estimates, which justify our approach

based on diapycnal mixing. Estimating the DWF rate by integrating a mixed patch volume from in situ measurements imposes the deployment of large-scale observations during the DWF event, which is intermittent in time, localized and is mostly characterized by strong winds and waves at surface, complicating work at sea from a research vessel. On the contrary, as diapycnal mixing is integral in time, it does not require high-frequency measurements. In addition, the diagnostic of DWF from tracers that interact with biology, such as O_2 or Chl_A is highly dependent on biological activity and implies strong hypotheses. Finally, satellite measurements such as altimetry provide high-frequency and high-resolution surface measurements, however their relation with DWF rate is not trivial *Herrmann et al.*, [2009].

The DWF estimate presented here is integrated in time, based on a physical diagnostic independent from biology and monitors the basin over all depths. This is why we strongly recommend the approach based on diapycnal mixing presented in this study to quantify DWF rate from observations.

6. Conclusions

An observing system simulation experiment (OSSE) has been proposed to estimate the dense water volume using the MOOSE network over the Northwestern Mediterranean (NWMed) Sea in the period 2012–2013 and its associated observation error. A yearly eddy-resolving simulation (SYMPHONIE, 1 km resolution) initialized in summer 2012 is used to estimate the spatiotemporal sampling and instrumental error of the observing network MOOSE carried out during four ship cruises in summer 2012, winter 2013, spring 2013, and summer 2013. Results show a low sampling error, with a 95% confidence level below 10% in all cases. It is maximum during winter when dense water thickness is most variable in space and time. This confirms the ability of MOOSE network to measure accurately the NWMed Sea dense water volume and its evolution in the period 2012–2013. On the other hand, the total sampling and instrumental error is comprised between 20% and 25% and it is dominated by the instrumental stability error, which reveals the importance of thoroughly calibrating CTD measurements in order to compute dense water volumes. An analytical relation between the space sampling error and the observation density is proposed, which reveals that space error falls below 10% when at least 50 observations are done and therefore that MOOSE network sampling is largely sufficient.

Open-sea dense water volumes are then estimated from observations. Results show that the dense water volumes have a strong seasonal cycle with a maximum during the spring 2013 cruise, and that dense water variations are dominated by transformations west of 6.5°E. Using the isopycnal $\sigma_0 = 29.11\ kg/m^3$ level, the dense water volume is relatively stable between summer 2012 ($13.3 \pm 0.6 \times 10^{13}\ m^3$) and winter 2013 ($13.7 \pm 1.3 \times 10^{13}\ m^3$), it increases dramatically in spring 2013 to $17.7 \pm 0.9 \times 10^{13}\ m^3$ and then it decreases rapidly to reach $15.1 \pm 0.6 \times 10^{13} m^3$ in summer 2013. The open-sea DWF rate is estimated between summer 2012 and spring 2013 and it reaches 1.4 ± 0.3 Sv, which is equivalent to 2.3 ± 0.5 Sv over the whole NWMed basin and during the deep convection period. This estimate is the highest ever observed DWF rate in the NWMed Sea, which suggests that 2012–2013 was an exceptional convective year. An analysis as a function of density reveals that half of the dense water is formed from the transformation of LIW and former dense water, and half from subsurface Atlantic waters. The open-sea restratification rate is estimated for the first time in the NWMed basin and it reaches between spring and summer 2013 -0.8 ± 0.4 Sv. It results mostly from the advection and mixing of deep waters whose average density decreases.

Appendix A: The Kriging Method

An assymetric kriging method is applied for the field reconstruction. For each model grid point, an assymetric Gaussian weight computed is given to the 10 closest observations (due to computational costs). In addition, no model guess is used in order to keep the volume estimates as independent from models as possible, so that they can be used for model validation purposes.

For each network and each period, a space correlogram is computed in order to fit a double Gaussian weight function for the field analysis. The correlation of all pairs of points within distance bins between 0 and 200 km is computed and shown in Figure 9 for SYMPHONIE simulation. The result is a spatial covariance function. A function is then fitted to the autocorrelation curve, which is the sum of two Gaussians involving two different spatial scales, with a least square method and ensuring a 100% autocorrelation at null

distance. The choice of two spatial scales ensures a high fit to the autocorrelation function ($r > 0.95$), which is not the case with only one scale (not shown). Figure 9a shows the autocorrelation function and Gaussian fit for SYMPHONIE simulation for the four cruise periods and their mean deduced from the virtual reality. The autocorrelation function is little sensitive to the period considered, with only SP13 cruise that has higher autocorrelation ranges on large scales. The mean autocorrelation function is fitted with two Gaussian functions of, respectively, 25 and 115 km ranges and almost same weight, with high accuracy.

The same autocorrelation and Gaussian fit with the undersampled field at MOOSE theoretical network shows different results (Figure 9b). The autocorrelation function is noisy due to the limited number of points used to construct it. In addition, the Gaussian fit gives mostly one dominant scale of 75 km in this case, which is an intermediate value between the two scales obtained with the virtual reality. This result shows that although a two-scale Gaussian fit seems adapted for the autocorrelation function, the network induces errors in their estimation and therefore in the kriging method. This source of error is part of the error related to space sampling and it is taken into account implicitly in this study. The double Gaussian weight function is hereafter deduced from virtual networks and not from the virtual reality to mimic actual estimates from the data only.

In addition, in a geostrophic approximation, water columns are expected to move as Taylor columns with a constant ratio *f/H*, with f the planetary vorticity and H bathymetry. Therefore, asymmetry across *f/H* contours is accounted for [see *Bohme and Send*, 2005, for a similar *f/H* asymmetry in kriging]. The relative distance to each observation is thus the product of the absolute distance between the points and the ratio of the *f/H* values at these points. For instance, an observation at 15 km distance and with a *f/H* twice as high (or twice lower) will be affected a relative distance of $15 \times 2 = 30$ km. Finally, the formula of the weight function is given by the equation:

$$W(X_1, X_2) = A\exp\left(-\frac{(d(X_1, X_2)R)^2}{p_1^2}\right) + (1-A)\exp\left(-\frac{(d(X_1, X_2)R)^2}{p_2^2}\right)$$

with

$$R = \max\left(\frac{f/H(X_1)}{f/H(X_2)}, \frac{f/H(X_2)}{f/H(X_1)}\right),$$

X_1 and X_2 are two locations, $d(X_1, X_2)$ is their absolute distance, p_1 and p_2 are the two Gaussian ranges deduced from each correlogram, A is the amplitude for the first range, *f/H* the ratio of the Coriolis parameter over bathymetry and R the *f/H* ratio between X_1 and X_2.

The analysis is done on a regular 1/10° grid in order to reduce computational costs. Due to the large autocorrelation scales ($p_1 = 25$ km and $p_2 = 115$ km), one expects little sensitivity of results to interpolation grid size δx as long as $\delta x < p$. For W13 ship cruise, a sensitivity of the OSSE on the analysis grid has been done which shows that results are little affected by the interpolation method (not shown here).

Acknowledgments

This work is a contribution to the HyMeX program (*HYdrological cycle in the Mediterranean EXperiment*—www.hymex.org) through INSU-MISTRALS support and through the ASICS-MED project (*Air-Sea Interaction and Coupling with Submesoscale structures in the MEDiterranean*, ANR-2012-BS06-003). The data used in this study are included in the references: *Testor et al.* [2012], *Testor* [2013], *Testor et al.* [2013], *Conan* [2013], and *Taillandier* [2014]. The authors thank the programmes HyMeX, MerMex, MOOSE, DEWEX, and the ANR project ASICS-Med for providing the funding necessary for this study. The authors are thankful for the recommendations formulated by the two anonymous reviewers, as well as the helpful exchanges with Gabriel Jordà.

References

Alvarez, A., and B. Mourre (2014), Cooperation or coordination of underwater glider networks? An assessment from observing system simulation experiments in the Ligurian sea, *J. Atmos. Oceanic Technol.*, *31*(10), 2268–2277.

Auger, P., C. Estournel, C. Ulses, L. Stemmann, S. Somot, and F. Diaz (2014), Interannual control of plankton ecosystem in a deep convection area as inferred from a 30-year 3D modeling study: Winter mixing and prey/predator interactions in the NW Mediterranean, *Prog. Oceanogr.*, *124*, 12–27, doi:10.1016/j.pocean.2014.04.004.

Ballabrera-Poy, J., E. Hackert, R. Murtugudde, and A. J. Busalacchi (2007), An observing system simulation experiment for an optimal moored instrument array in the tropical Indian ocean, *J. Clim.*, *20*(13), 3284–3299.

Béranger, K., Y. Drillet, M.-N. Houssais, P. Testor, R. Bourdallé-Badie, B. Alhammoud, A. Bozec, L. Mortier, P. Bouruet-Aubertot, and M. Crépon (2010), Impact of the spatial distribution of the atmospheric forcing on water mass formation in the Mediterranean Sea, *J. Geophys. Res.*, *115*, C12041, doi:10.1029/2009JC005648.

Bethoux, J.-P. (1980), Mean water fluxes across sections in the Mediterranean sea, evaluated on the basis of water and salt budgets and of observed salinities, *Oceanol. Acta*, *3*(1), 79–88.

Béthoux, J.-P., X. Durrieu de Madron, F. Nyffeler, and D. Tailliez (2002), Deep water in the western Mediterranean: Peculiar 1999 and 2000 characteristics, shelf formation hypothesis, variability since 1970 and geochemical inferences, *J. Mar. Syst.*, *33–34*, 117–131.

Beuvier, J., K. Branger, C. L. Brossier, S. Somot, F. Sevault, Y. Drillet, R. Bourdall-Badie, N. Ferry, and F. Lyard (2012), Spreading of the western Mediterranean deep water after winter 2005: Time scales and deep cyclone transport, *J. Geophys. Res.*, *117*, C07022, doi:10.1029/2011JC007679.

Bohme, L., and U. Send (2005), Objective analyses of hydrographic data for referencing profiling float salinities in highly variable environments, *Deep Sea Res., Part II*, *52*, 651–664.

Bosse, A., P. Testor, L. Mortier, L. Prieur, V. Taillandier, F. d'Ortenzio, and L. Coppola (2015), Spreading of Levantine intermediate waters by submesoscale coherent vortices in the northwestern Mediterranean sea as observed with gliders, *J. Geophys. Res. Oceans*, *120*, 1599–1622, doi:10.1002/2014JC010263.

Canals, M., P. Puig, X. Durrieu de Madron, S. Heussner, A. Palanques, and J. Fabres (2007), Flushing submarine canyons, *Nature*, *444*, 354–357.
Castellari, S., N. Pinardi, and K. Leaman (2000), Simulation of the water mass formation processes in the Mediterranean Sea: Influence of the time frequency of the atmospheric forcing, *J. Geophys. Res.*, *105*(C10), 24,157–24,181, doi:10.1029/2000JC900055.
Conan, P. (2013), Dewex-mermex 2013 leg2 cruise, le suroit r/v, *Tech. Rep.*, doi:10.17600/13020030. [Available at http://campagnes.flotteoceanographique.fr/campagnes/13020030/.]
Crépon, M., M. Boukthir, B. Barnier, and F. Aikman III (1989), Horizontal ocean circulation forced by deep-water formation. Part I: An analytical study, *J. Phys. Oceanogr.*, *19*, 1781–1792.
Demirov, E. K., and N. Pinardi (2007), On the relationship between the water mass pathways and eddy variability in the western Mediterranean sea, *J. Geophys. Res.*, *112*, C02024, doi:10.1029/2005JC003174.
D'Ortenzio, F., D. Iudicone, C. de Boyer Montegut, P. Testor, D. Antoine, S. Marullo, R. Santoleri, and G. Madec (2005), Seasonal variability of the mixed layer depth in the Mediterranean Sea as derived from in situ profiles, *Geophys. Res. Lett.*, *32*, L12605, doi:10.1029/2005GL022463.
Durrieu de Madron, X., et al. (2013), Interaction of dense shelf water cascading and open-sea convection in the northwestern Mediterranean during winter 2012, *Geophys. Res. Lett.*, *40*, 1379–1385, doi:10.1002/grl.50331.
Estournel, C., V. Zervakis, P. Marsaleix, A. Papadopoulos, F. Auclair, L. Perivoliotis, and E. Tragou (2005), Dense water formation and cascading in the Gulf of Thermaikos (North Aegean) from observations and modelling, *Cont. Shelf Res.*, *25*, 2366–2386, doi:10.1016/j.csr.2005.08.014.
Estournel, C., et al. (2016), High resolution modeling of dense water formation in the north-western mediterranean during winter 2012–2013: Processes and budget, *Journal of Geophysical Research: Oceans*, *121*(7), 5367–5392, doi: 10.1002/2016JC011935.
Groeskamp, S., J. D. Zika, T. J. McDougall, B. M. Sloyan, and F. Laliberté (2014a), The representation of ocean circulation and variability in thermodynamic coordinates, *J. Phys. Oceanogr.*, *44*(7), 1735–1750.
Groeskamp, S., J. D. Zika, B. M. Sloyan, T. J. McDougall, and P. C. McIntosh (2014b), A thermohaline inverse method for estimating diathermohaline circulation and mixing, *J. Phys. Oceanogr.*, *44*, 2681–2697, doi:10.1175/JPO-D-14-0039.1.
Hackert, E. C., R. N. Miller, and A. J. Busalacchi (1998), An optimized design for a moored instrument array in the tropical Atlantic ocean, *J. Geophys. Res.*, *103*(C4), 7491–7509, doi:10.1029/97JC03206.
Hamon, M., et al. (2016), Design and validation of Medrys, a Mediterranean sea reanalysis over the period 1992–2013, *Ocean Sci.*, *12*(2), 577–599, doi:10.5194/os-12-577-2016.
Herrmann, M., and S. Somot (2008), Relevance of ERA40 dynamical downscaling for modeling deep convection in the Mediterranean Sea, *Geophys. Res. Lett.*, *35*, L04607, doi:10.1029/2007GL032442.
Herrmann, M., S. Somot, F. Sevault, C. Estournel, and M. Déqué (2008a), Modeling the deep convection in the Northwestern Mediterranean sea using an eddy-permitting and an eddy-resolving model: Case study of winter 1986–87, *J. Geophys. Res.*, *113*, C04011, doi:10.1029/2006JC003991.
Herrmann, M., C. Estournel, M. Déqué, P. Marsaleix, F. Sevault, and S. Somot (2008b), Dense water formation in the Gulf of Lions shelf: Impact of atmospheric interannual variability and climate change, *Cont. Shelf Res.*, *28*(15), 2092–2112, doi:10.1016/j.csr.2008.03.003.
Herrmann, M., J. Bouffard, and K. Béranger (2009), Monitoring open-ocean deep convection from space, *Geophys. Res. Lett.*, *36*, L03606, doi:10.1029/2008GL036422.
Herrmann, M., F. Sevault, J. Beuvier, and S. Somot (2010), What induced the exceptional 2005 convection event in the northwestern Mediterranean basin? Answers from a modeling study, *J. Geophys. Res.*, *115*, C08029, doi:10.1029/2009JC005749.
Herrmann, M., F. Diaz, C. Estournel, P. Marsaleix, and C. Ulses (2013), Impact of atmospheric and oceanic interannual variability on the Northwestern Mediterranean Sea pelagic planktonic ecosystem and associated carbon cycle, *J. Geophys. Res.*, *118*, 5792–5813, doi:10.1002/jgrc.20405.
Lascaratos, A. (1993), Estimation of deep and intermediate water mass formation rates in the Mediterranean sea, *Deep Sea Res., Part II*, *40*(6), 1327–1332.
L'Hévéder, B., L. Li, F. Sevault, and S. Somot (2013a), Interannual variability of deep convection in the northwestern Mediterranean simulated with a coupled AORCM, *Clim. Dyn.*, *41*(3–4), 937–960, doi:10.1007/s00382-012-1527-5.
L'Hévéder, B., L. Mortier, P. Testor, and F. Lekien (2013b), A glider network design study for a synoptic view of the oceanic mesoscale variability, *J. Atmos. Oceanic Technol.*, *30*(7), 1472–1493.
Madec, G., M. Chartier, P. Delecluse, and M. Crépon (1991), A three-dimensional numerical study of deep-water formation in the Northwestern Mediterranean Sea, *J. Phys. Oceanogr.*, *21*(9), 1349–1371.
Marsaleix, P., F. Auclair, and C. Estournel (2009), Low-order pressure gradient schemes in sigma coordinate models: The seamount test revisited, *Ocean Modell.*, *30*, 169–177, doi:10.1016/j.ocemod.2009.06.011.
Marsaleix, P., F. Auclair, C. Estournel, C. Nguyen, and C. Ulses (2012), Alternatives to the Robert-Asselin filter, *Ocean Modell.*, *41*, 53–66, doi:10.1016/j.ocemod.2011.11.002.
Marshall, J., and F. Schott (1999), Open-ocean convection: Observations, theory, and models, *Rev. Geophys.*, *37*(1), 1–64.
Mertens, C., and F. Schott (1998), Interannual variability of deep-water formation in the Northwestern Mediterranean, *J. Phys. Oceanogr.*, *28*, 1410–1424.
Mourre, B., P. Mey, Y. Ménard, F. Lyard, and C. Provost (2006), Relative performance of future altimeter systems and tide gauges in constraining a model of north sea high-frequency barotropic dynamics, *Ocean Dyn.*, *56*(5), 473–486, doi:10.1007/s10236-006-0081-2.
Naranjo, C., J. Garcia-Lafuente, G. Sannino, and J. C. Sanchez-Garrido (2014), How much do tides affect the circulation of the Mediterranean sea? From local processes in the strait of Gibraltar to basin-scale effects, *Prog. Oceanogr.*, *127*, 108–116.
Pinardi, N., et al. (2013), Mediterranean sea large-scale low-frequency ocean variability and water mass formation rates from 1987 to 2007: A retrospective analysis, *Prog. Oceanogr.*, *132*, 318–332.
Rhein, M. (1995), Deep water formation in the western Mediterranean, *J. Geophys. Res.*, *100*(C4), 6943–6959, doi:10.1029/94JC03198.
Rugenstein, M., M. Winton, R. J. Stouffer, S. M. Griffies, and R. Hallberg (2013), Northern high-latitude heat budget decomposition and transient warming, *J. Clim.*, *26*, 609–621.
Santinelli, C., D. A. Hansell, and M. Ribera d'Alcalà (2013), Influence of stratification on marine dissolved organic carbon (doc) dynamics: The Mediterranean sea case, *Prog. Oceanogr.*, *119*, 68–77.
Schroeder, K., A. Ribotti, M. Borghini, R. Sorgente, A. Perilli, and G. P. Gasparini (2008a), An extensive western Mediterranean deep water renewal between 2004 and 2006, *Geophys. Res. Lett.*, *35*, L18605, doi:10.1029/2008GL035146.
Schroeder, K., M. Borghini, G. Cerrati, V. Difesca, R. Delfanti, C. Santinelli, and G. Gasparini (2008b), Multiparametric mixing analysis of the deep waters in the western Mediterranean sea, *Chem. Ecol.*, *24*, 47–56.

Somot, S., F. Sevault, and M. Déqué (2006), Transient climate change scenario simulation of the Mediterranean Sea for the 21st century using a high resolution ocean circulation model, *Clim. Dyn.*, *27*, 851–879, doi:10.1007/s00382-006-0167-z.

Somot, S., et al. (2016), Modelling and understanding the climate variability of the deep water formation in the north-western mediterranean sea, *Climate Dynamics*, doi: 10.1007/s00382-016-3295-0, in press.

Taillandier, V. (2014), (ctd dataset acquired during the field survey dewex), *Tech. Rep.*, doi:10.17600/13450110. [Available at ftp://oceane.obs-vlfr.fr/pub/prieur/GC/Dewex2013leg1_leg2_ASCII/DEWEX2013-CTDreport.pdf.]

Tamburini, C., et al. (2013), Deep-sea bioluminescence blooms after dense water formation at the ocean surface, *PLoS ONE*, *8*(7), e67523, doi:10.1371/journal.pone.0067523.

Testor, P. (2013), Dewex-mermex 2013 leg1 cruise, le suroit r/v, *Tech. Rep.*, doi:10.17600/13020010. [Available at http://campagnes.flotteoceanographique.fr/campagnes/13020010/.]

Testor, P., and J.-C. Gascard (2006), Post-convection spreading phase in the Northwestern Mediterranean Sea, *Deep Sea Res., Part I*, *53*, 869–893.

Testor, P., L. Coppola, and L. Mortier (2012), (2012 moose-ge cruise, le suroit r/v), *Tech. Rep.*, doi:10.17600/12020030. [Available at http://campagnes.flotteoceanographique.fr/campagnes/12020030/index.htm.]

Testor, P., L. Coppola, and L. Mortier (2013), (2013 moose-ge cruise, tethys ii r/v), *Tech. Rep.*, doi:10.17600/13450110. [Available at http://campagnes.flotteoceanographique.fr/campagnes/13450110/index.htm.]

Tziperman, E., and K. Speer (1994), A study of water mass transformation in the Mediterranean Sea: Analysis of climatological data and a simple three-box model, *Dyn. Atmos. Oceans*, *21*, 53–82.

Ulses, C., C. Estournel, P. Puig, X. Durrieu de Madron, and P. Marsaleix (2008), Dense shelf water cascading in the northwestern Mediterranean during the cold winter 2005. Quantification of the export through the Gulf of Lion and the Catalan margin, *Geophysical Res. Lett.*, *35*, L07610, doi:10.1029/2008GL033257.

Visbeck, M. J., J. Marshall, and H. Jones (1996), Dynamics of isolated convective regions in the ocean, *J. Phys. Oceanogr.*, *26*, 1721–1734.

Walin, G. (1982), On the relation between sea-surface heat flow and the thermal circulation in the ocean, *Tellus*, *34*, 187–195.

Winton, M., S. M. Griffies, B. L. Samuels, J. L. Sarmiento, and T. L. Frolicher (2013), Connecting changing ocean circulation with changing climate, *J. Clim.*, *26*, 2268–2278.